ADVANCED ENERGY MATERIALS
www.advenergymat.de

Rapid Scalable One-step Production of Catalysts for Low-Iridium Content Proton Exchange Membrane Water Electrolyzers

Suriya Venkatesan, Jens Mitzel, Sambal Shashank Ambu, Tobias Morawietz, Indro Biswas, Oscar Recalde, Esmaeil Adabifiroozjaei, Leopoldo Molina-Luna, Deven P. Estes, Karsten Wegner, Pawel Gazdzicki, Aldo Saul Gago, and Kaspar Andreas Friedrich*

Proton exchange membrane water electrolysis (PEMWE) is a promising technology for green hydrogen production, although its widespread development with state-of-the-art loadings is threatened by the scarcity of iridium (Ir). Homogeneous dispersion of Ir in an immiscible electro-ceramic matrix can enhance catalytic mass activity and structural stability. The study presents $Ir_ySn_{0.9(1-y)}Sb_{0.1(1-y)}O_x$ solid solutions produced by highly scalable flame spray pyrolysis (FSP) process as efficient anode electrocatalysts for PEMWE, containing only 0.2 mg cm^{-2} of Ir in the catalyst layer (CL). Intense mixing of metal vapor and large thermal gradients in the precursor-derived high-temperature flame aids stabilizing sub-nanoscale entropic mixing within self-preserved 4–6 nm particles. Detailed investigations confirm that the one-step prepared solid solution electrocatalysts exhibit up to fourfold higher activity toward the oxygen evolution reaction (OER) compared to Ir black. The anode of a PEMWE utilizing this catalyst exhibits high performance and stability over 2000 h but with tenfold lower Ir loading than the state-of-art.

1. Introduction

The European Green Deal and the US Inflation Reduction Act have emphasized clean tech products, including hydrogen production from renewable energy through power-to-gas processes.[1,2] Among the electrolysis technologies, PEMWE stands out due to its high-power density, making it well-suited for advancing the decarbonizing hydrogen economy. However, TW-scale PEMWE installation may be limited by the high cost (148 € g^{-1} in 2023) and scarcity and limited mining availability of Ir (0.003 ppb in the earth's crust), which serves as the main catalyst for the OER.[3,4] Currently, commercial systems typically require a Ir loading of

S. Venkatesan, J. Mitzel, S. S. Ambu, T. Morawietz, I. Biswas, P. Gazdzicki, A. S. Gago, K. A. Friedrich
Department of Electrochemical Energy Technology
Institute of Engineering Thermodynamics
German Aerospace Centre (DLR)
70569 Stuttgart, Germany
E-mail: aldo.gago@dlr.de

S. Venkatesan, S. S. Ambu, K. A. Friedrich
Institute of Building Energetics
Thermal Engineering and Energy Storage (IGTE)
University of Stuttgart
70569 Stuttgart, Germany

S. S. Ambu
Cutting-Edge Nanomaterials (CENmat)
75181 Pforzheim, Germany

The ORCID identification number(s) for the author(s) of this article can be found under https://doi.org/10.1002/aenm.202401659

DOI: 10.1002/aenm.202401659

T. Morawietz
Faculty of Science
Energy and Building Services
Esslingen University of Applied Sciences
73728 Esslingen am Neckar, Germany

O. Recalde, E. Adabifiroozjaei, L. Molina-Luna
Advanced Electron Microscopy Division
Department of Materials-and Geosciences
Technical University Darmstadt
64287 Darmstadt, Germany

D. P. Estes
Institute of Technical Chemistry
University of Stuttgart
70569 Stuttgart, Germany

K. Wegner
Department of Mechanical and Process Engineering
Particle Technology Laboratory
ETH Zurich, Zurich 8092, Switzerland

K. Wegner
ParteQ GmbH
76316 Malsch, Germany

2 to 2.5 mg cm^{-2} at the anode to enable the kinetically sluggish OER.[5] However, to meet global H_2 demand today (≈400 GW), the Ir loading needs to be reduced at least tenfold, assuming that 20% of the annual Ir production (10^4 kg a^{-1}) is diverted to PEMWE for 10 years.[5] Efforts are underway to reduce the Ir content by investigating modified catalyst structures such as semiconducting metal oxide-supported Ir oxides[6–8] and Ir-containing mixed oxides[9,10] that enable efficient utilization of Ir. These catalytically inactive secondary oxides enhance Ir mass activity for OER at lower potentials by donating electrons or suppress overoxidation and passivation of Ir at higher anodic potentials through the migrating oxygen species.[11]

For supported Ir oxides, supports such as Sb, Nb, Ta, F, or In-doped SnO_2 and TiO_2 have been identified as suitable candidates.[12] However, reducing the Ir concentration in the composition below 50 wt.% – the current state-of-the-art – necessitates the formation of a network of crystalline Ir species to ensure sufficient in-plane electrical conductivity and corrosion resistance.[6,13] Thus, stabilizing finely dispersed nanoparticles containing Ir is crucial for enhancing the durability of PEMWE.[7] Consequently, most studies have focused on thin layers of Ir, IrO_x or Ir-O-$(OH)_x$ on calcined-supports using wet-chemical methods. This typically involves creating functional groups on the support surface, followed by thermal annealing to control the degree of surface amorphization.[6,7,11,14] Besides reducing the electrochemically active surface area (ECSA) and/or the conductance of the supporting oxides,[15] separating the production of support and catalyst may weaken the catalyst-support interaction, potentially limiting the homogeneous and stable anchoring of Ir onto the supports.

An alternative approach to alleviate these constraints is the utilization of Ir-based solid solutions or Ir-containing mixed oxides (e.g., $Ir_xTa_{1-x}O_{2.45}$,[10] $Ir_xSn_{1-x}O_2$,[16–18] high entropy electrocatalysts,[19] Ir-based perovskites,[9] and $SrIr_xZn_{1-x}O_3$[20]). These materials may exhibit synergetic effects and lattice-strain-induced enhancements in intrinsic OER activity, making them attractive alternatives for efficient Ir utilization.[21] Additionally, the difference in atomic sizes increases the energy barrier for the diffusion of elements and their dissolution into corrosive solutions.[19] The presence of less noble metal neighbors in these structures allows tuning the d-band position and electronic structure of active sites, thereby the adsorption strength of the OER intermediates.[12] However, challenges such as structural instability in acidic conditions,[9] phase segregation during thermal treatments,[22] and noble metal agglomeration within the particle core,[23] influenced by both the synthesis method and the thermodynamics and kinetics of nanoparticle formation, remain significant concerns. These issues can adversely affect cell performance and durability, particularly at lower Ir loadings.

Furthermore, synthesis procedures for such catalysts are currently at the level of grams per hour and involve numerous steps, far from the requirements of catalyst production for GW-scale PEMWE. In fact, most of the reported synthesis methods are neither scalable nor economically viable. They require multiple energy-intensive steps such as chemical reduction of Ir precursors, mixture chemical reduction, filtration, purification, and thermal treatment. In the case of supported Ir catalysts such as Ir/SnO_2:Sb, the situation is even more disadvantageous as the support needs to be synthetized separately involving as many steps as the production of IrO_2.

In general, doping of SnO_2 with antimony (ATO), fluorine (FTO), and indium (ITO) atoms has been shown to be a successful strategy to enhance conductivity whereas the stability of doped-tin iridium oxide catalysts is still to be clarified.[24] Here, we aim to combine the superior conductivity of the antimony doped tin oxide system with highly dispersed Ir with most atoms in Ir^{3+}/Ir^{4+} oxidation states, which has been reported to provide high activity,[9] using flame spray pyrolysis (FSP) as a suitable synthesis method. ATO was selected as the carrier for Ir species dispersion due to its lower environmental impact and relatively higher performance as compared to FTO and ITO, respectively.

FSP is a resource-lean gas-phase synthesis technique for rapid and efficient production of materials in one-step.[25] Using an appropriate precursor solution, multicomponent nanoparticles can be synthesized without phase segregation. The precursor solution that also provides the majority of the total enthalpy of the system, is atomized in a spray flame where droplets undergo a series of micro-explosions.[26] Nuclei typically evolve from the gas-phase and grow by collision-sintering within microseconds leading to intense atomic-scale mixing of the different elements. The unique thermal characteristics of the flame, namely temperatures up to 3000 °C and rapid cool-down, aid stabilizing phases, including metastable phases in a non-equilibrium arrangement, and promote crystallinity at the nanoscale. The ability of FSP to produce multi-component nanomaterials at lab-scale up to industrial-scale in a continuous process without thermal and chemical gradients cannot be matched by conventional methods.[27] This enables the high-throughput screening of challenging multi-component structures. For further information on flame synthesis of electrocatalysts and its advantages over conventional chemical synthesis (e.g., co-precipitation, direct thermal pyrolysis, sol–gel, hydrothermal, citrate method, spray pyrolysis), as well as reactive powder processing, and direct thermal pyrolysis, we refer to our review article.[27] The use of such a scalable and resource-lean method for producing challenging electrocatalyst is vital for bridging the gap between electrode material development and optimization of cell-and stack-level performance and stability, thereby facilitating the fast commercialization of PEMWE without the need for numerous stages of scale-up and fundamental catalyst testing.

Herein, we present for the first-time the rapid scalable one-step production of catalyst solid solutions of $Ir_\gamma Sn_{0.9(1-\gamma)}Sb_{0.1(1-\gamma)}O_x$ (γ is 0.37 or 0.51, corresponding to 35 or 50 wt.% Ir, respectively) via the FSP process. The electrode material has proven to be a high-performance and stable electrocatalyst, enabling a reduction in Ir content in the anode of a PEMWE cell to 0.2 mg cm^{-2} under industrial relevant conditions, ≈10 times lower than current commercial systems.

2. Results and Discussion

$Ir_{0.37}Sn_{0.57}Sb_{0.06}O_x$ (hereafter referred to as 37-ISS) and $Ir_{0.51}Sn_{0.44}Sb_{0.05}O_x$ (denoted as 51-ISS) nanoparticles with tailored compositions were prepared using FSP (**Figure 1a**; Table S1, Supporting Information). Precursor solutions containing carboxylic metal salts $MC_xH_yO_z$ (where M represents Sb, Sn, and/or Ir) dissolved in a 3:1 mixture of xylenes and

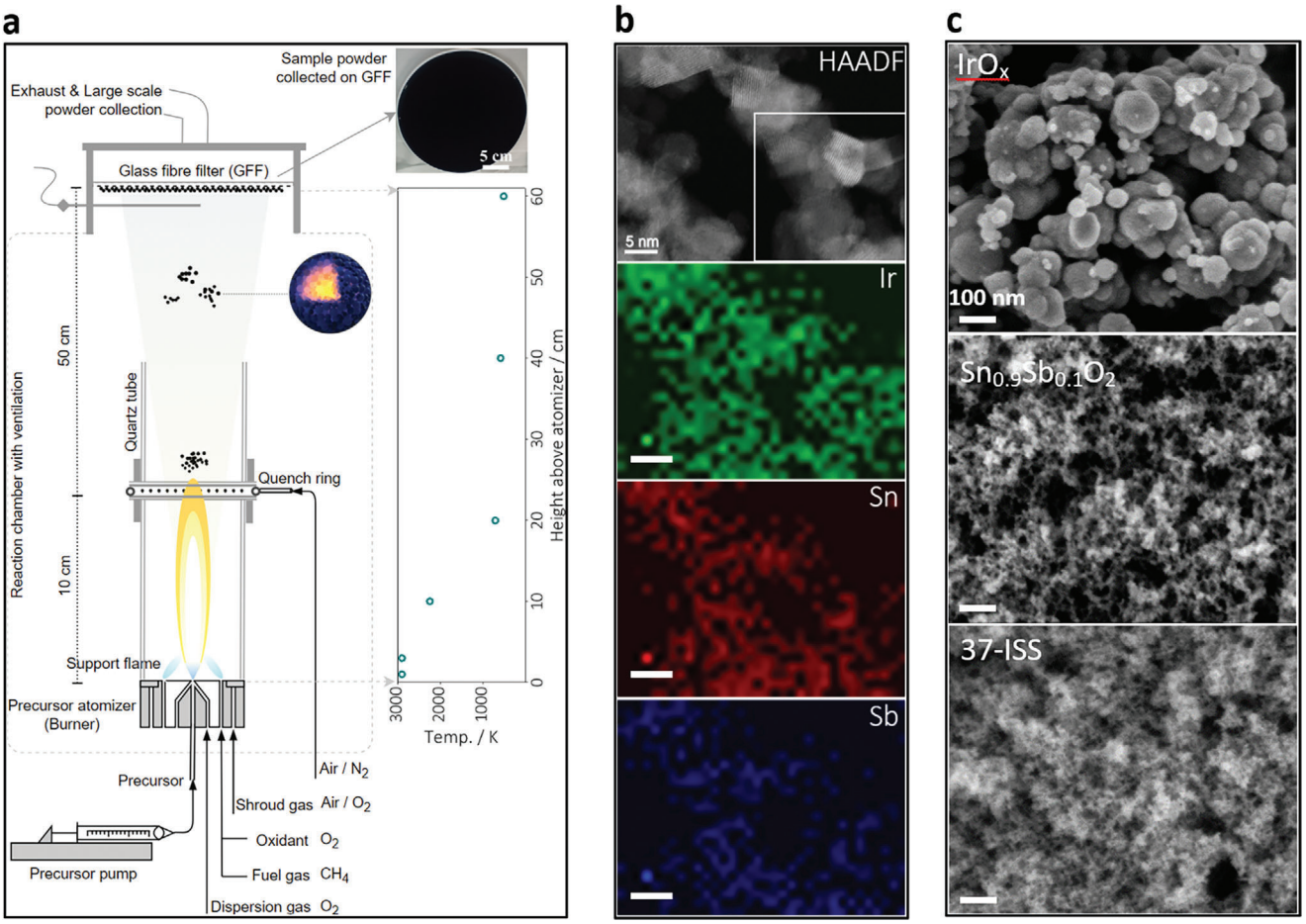

Figure 1. a) Schematic of the FSP setup. The catalyst powder is collected using the glass fiber filter shown at the top right. The temperature profile of a typical flame using 5 mL min^{-1} precursor and 5 L min^{-1} dispersion gas flow rates shown at the right. b) HAADF image of as-synthesized 37-ISS with the area marked for elemental maps of Ir, Sn, and Sb. c) In-lens SEM images of as-synthesized IrO_x, $Sn_{0.9}Sb_{0.1}O_2$, and 37-ISS.

diethylene glycol butyl ether were prepared with a final metal concentration of 50 mM and atomized at 5 mL min^{-1} with 8 L min^{-1} O_2 dispersion gas. The spray was ignited by a premixed support flame (1 L min^{-1} CH_4, 3 L min^{-1} O_2), generating a high-temperature spray flame – the reactor – where catalyst nanoparticles are produced within milliseconds in one step,[27] before collection on glass fiber filter disks. In a typical synthesis experiment, the flame reached a maximum temperature of ≈2900 K at ≈2 cm above the atomizer, while it was only ≈513 K at the filter positioned 60 cm above the atomizer, indicating rapid cooling at ≈150 K cm^{-1} (corresponding to 10^5–10^6 K s^{-1}) (Figure 1a). In another experiment, the cooling rate of the flame aerosol was intensified by introducing 60 L min^{-1} of air at the flame tip (see Figure 1a). The sample was denoted as 51-ISS-Q, with Q indicating quenching. This quenching process halted further catalyst evolution. To ensure complete combustion of carbon species from the precursor, 80 L min^{-1} of shroud air was introduced around the otherwise enclosed flame. The resulting electrocatalyst nanopowders, collected from the filter without additional processing steps, were utilized to prepare catalyst-coated membranes (CCM) with an Ir loading of 0.2 mg cm^{-2} for PEMWE. Thus, complex Ir catalyst particles can be synthesized via FSP in one single step and used right after for the PEMWE application. The compositions of the solvent mixture and the premixed support flame used in this study were adopted from previously established protocols for metal oxide nanoparticle synthesis using FSP.[28] It should be noted that the lab-scale FSP set up used in this study employs a glass fiber filter disk (257 mm diameter) to collect particles directly above the flame. The production time for a small batch of 1 g of electrocatalyst was 15 min plus ≈10 min for product particle recovery and sieving. FSP has been systematically scaled up to 500 g h^{-1} and pilot-scale FSP systems that continuously produce nanoparticles at kg h^{-1} level have been realized, utilizing baghouse filters for nanopowder collection.[29]

The elemental maps (Figure 1b) of 37-ISS measured using energy dispersive x-ray analysis (EDX) revealed no apparent elemental segregation. The high-angle annular dark-field (HAADF) image, where contrast is proportional to the atomic number, further confirmed the predominantly uniform mixing of all three elements at the sub-nanometer scale (Figure 1b). Unlike Sb, Ir is expected to be immiscible with Sn due to differences in empirical atomic radius (1.35 vs. 1.45Å), surface energy, redox potential, and the preferential structure of their oxide and metallic

forms, as reflected in the equilibrium phase diagram.[30] However, the intense mixing of species due to numerous coagulation and condensation events within the high-temperature flame, followed by intrinsic rapid quenching, appears to enable kinetic control over thermodynamic mixing process. This approach suppresses atomic mobility, thereby stabilizing a predominantly single-phase, homogeneous solid solution of Ir with Sn and Sb in a non-equilibrium process, similar to carbothermal shock synthesis of high-entropy-alloy nanoparticles, but with the added benefit of high scalability.[31]

The nanoparticles maintained a size uniformity with diameters of (6.0 ± 1.8) nm (Figure S1d obtained from Figure 1b; Figure S1a, Supporting Information), along with a high degree of crystallinity as shown in fast Fourier transform (FFT) images (Figure S1b, Supporting Information). In contrast, recent attempts to synthesize $Ir_xRu_{1-x}O_y$ as an OER electrocatalyst using FSP[32] and a similar technique called reactive spray deposition techniques[33,34] resulted in amorphous structures with very short-range crystalline order, necessitating an additional calcination step.[32] This significant discrepancy between 37-ISS and $Ir_xRu_{1-x}O_y$ suggests a difference in particle formation mechanisms. To investigate this, IrO_x, $Sn_{0.9}Sb_{0.1}O_2$, 37-ISS and 51-ISS were prepared using identical FSP protocols. Scanning electron microscopy (SEM) images in Figure 1c (top) reveal that pure IrO_x forms aggregates of primary particles with a broad size distribution ranging from 10 to 130 nm. This behavior can be attributed to the dissociation of IrO_2 in air at ≈1020 °C, analogous to RuO_2 at ≈1405 °C.[35] Consequently, metallic Ir particles are likely present in the flame core that coalesce rapidly upon collisions, forming relatively large entities. As the flame temperature decreases, oxide formation progresses and sintering ceases, leading to the observed aggregates with primary particles up to 130 nm (Figure 1c, top). On the contrary, $Sn_{0.9}Sb_{0.1}O_2$ exhibits much smaller primary particle sizes of (5.30 ± 0.83) nm (Figure S1d, Supporting Information) that are similar to the average crystallite size (4.46 ± 0.62) nm, proving that the primary particles are single crystals. Unlike IrO_x, Sn,[30] and Sb[36] oxides do not dissociate in the flame. The small primary particle size of $Sn_{0.9}Sb_{0.1}O_2$, along with its fractal-like agglomerate structure (Figure 1c, middle) indicate that these particles sinter more slowly upon collisions compared to metallic iridium (or ruthenium). A similar morphology of 37-ISS as $Sn_{0.9}Sb_{0.1}O_2$ indicates that the presence of the oxides apparently slows down primary particle growth upon collisions also for the Ir-Sn-Sb-O_2 system. Despite the differing particle formation pathways of IrO_x and $Sn_{0.9}Sb_{0.1}O_2$, the $Sn_{0.9}Sb_{0.1}O_2$-like characteristics observed in 37-ISS suggest a preference for not only random alloying but also substitution mechanisms. This is evident from a defect-rich surface and a disordered lattice structure (OH^- adsorption sites), which likely arise from the synergistic effects of high temperature and cationic doping (Figure S1e, Supporting Information).

The electronic structure and surface properties of the FSP products were analyzed via X-ray photoelectron spectroscopy (XPS) (**Figure 2a,b**; Figure S2, Supporting Information). The Ir4f XPS spectra of 37-ISS and 51-ISS (Figure 2a) were compared with commercially available IrO_2 (Figure S2a, Supporting Information). The $Ir4f_{7/2}$ signal of 37-ISS exhibits an additional contribution beyond the typical binding energy of 62.05 eV, complicating the precise differentiation between Ir^{5+} and Ir^{6+} states. It can only be numerically described by the abundant contribution at ≈62.65 and ≈63.85 eV components, implying the likely presence of higher valence Ir species[9] or proximity to oxygen vacancies.[37] Similarly, 51-ISS shows analogous characteristics but with a binding energy[38] shift of −0.4 eV, which can be attributed to disorder-induced loss of lattice oxygen.

The deconvoluted O1s spectrum (Figure 2b) reveals an increase in oxygen vacancy and surface adsorbed oxygen by ca. 4.6% and 37.2%, respectively, with increased Ir content. The corresponding shift in the Ir4f signal to a lower value indicates the presence of more Ir^{4+} sites near oxygen vacancies. These vacancies are expected to regulate the electronic structure of 51-ISS and enhance the availability of OER active sites.[38] Similarly, the binding energies of $Sn3d_{5/2}$ are also shifted by −0.4 eV in 51-ISS (Figure S2c, Supporting Information) compared to 37-ISS and $Sn_{0.9}Sb_{0.1}O_2$, suggesting the distribution of electronic density[19] between Sn/Sb and Ir, and indicating homogenous coordination environments in this solid solution.

The Ir4f spectra for the as-synthesized samples exhibit characteristic asymmetric line shape profiles, which remain consistent regardless of the Ir content. This indicates that the core-level states of the rutile-type structures are largely stable and unaffected.[32] To further investigate the surface properties of the flame-synthesized materials, 37-ISS was calcined at 673 K for 1 h in air (Figure S2d, Supporting Information) prior to XPS analysis. The calcined sample displayed only a slight increase in the asymmetry of the line shape profile, with no significant changes compared to the as-synthesized sample. This confirms the robustness of the surface electronic states in the high temperature-derived structures and further supports their rutile nature. Based on the results, we anticipate high catalyst stability and minimal degradation during PEMWE operation.

X-ray adsorption near edge spectroscopy (XANES) at the Ir L3 edge was used to confirm the bulk Ir oxidation states of 37-ISS and 51-ISS by comparison with the standards of Ir black, $Ir(acac)_3$ and IrO_2 (Figure 2c; Figure S3, Supporting Information). The spectra show 'white line' peaks at ≈11220 eV and oscillations at higher photon energies due to interactions of the emitted electron wave with the neighboring atoms. The white line signals exhibit the typical dependence of intensity on the oxidation state with only small changes (<2 eV) in the position of the white line. The integrated intensities reveal a direct linear correlation of the number of unoccupied states in the d-band of the material with the white line intensity (Figure 2d), making the determination of the average bulk oxidation states of 37-ISS and 51-ISS possible. These correlations correspond to average oxidation states of 3.9 for 37-ISS and 3.6 for 51-ISS. This indicates that 51-ISS contains a higher proportion of reduced phases compared to 37-ISS, a finding consistent with the XPS observations.

X-ray diffraction (XRD) (Figure 2e) of the 37-ISS sample reveals peaks at $2\theta = 26.9°$, 34.3°, and 52.5°, which can be indexed to the (110), (101), and (211) planes of the predominant tetragonal rutile-type phase, respectively. The peak shift toward lower 2θ compared to pure rutile-IrO_2 is attributed to lattice expansion by accommodation of larger Sn atoms, induced by rapid cooling of the flame aerosol. This implies that the 37-ISS solid solution is the predominant phase. A smaller fraction of metallic Ir is also detected in 37-ISS, as well as in pure IrO_x and in 51-ISS (Figure S4, Supporting Information). However, the explicit

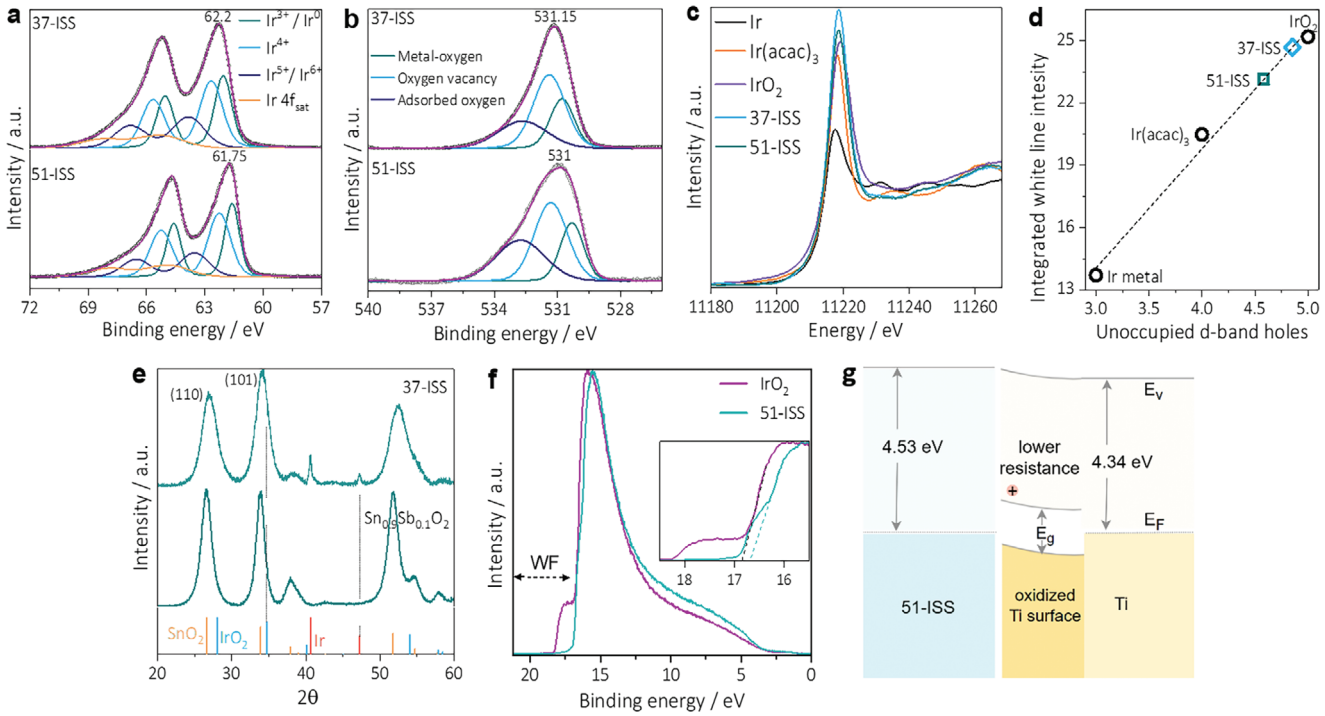

Figure 2. a) Deconvoluted Ir4f XPS spectra of 37-ISS and 51-ISS. b) Sb3d-subtracted and deconvoluted O1s XPS spectra of 37-ISS and 51-ISS. c) XANES. c) Ir L3-edge XANES spectra of Ir, $Ir(acac)_3$, IrO_2, 37-ISS, and 51-ISS. d) Plot of integrated white line intensity vs. number of unoccupied d-band holes. The fitted line is a linear regression of the Ir, $Ir(acac)_3$, and IrO_2 Standards. Positions of the 37-ISS and 51-ISS indicated on this scale. e) XRD patterns of $Sb_{0.9}Sn_{0.1}O_2$ and 51-ISS. Reference Ir, IrO_2, and SnO_2 patterns from ICDD card numbers 00-006-0598 (red), 00-015-0870 (blue), and 00-041-1445 (orange), respectively. f) Ultraviolet photoelectron spectroscopy (UPS) spectra for IrO_2 and 51-ISS, and g) Energy band diagram for 51-ISS and oxidized Ti PTL interface.

incorporation of an Ir^0 doublet in the XPS spectral deconvolution (Figure 2a) reveals no significant contribution (<3%), which is well within the possible error margin. Considering the size of the catalyst particles (<7 nm), which is comparable to the information depth of ≈8.25 nm (corresponding to an inelastic mean free path of the emitted Iridium 4f electrons of ≈2.75 nm at the used X-ray photon energy of 1486 eV), it can be inferred that any metallic Ir, if present, is insignificant and well dispersed at the subsurface. Scanning TEM (STEM) images of the 51-ISS reveal a fraction of phase-separated pure $Sn_{0.9}Sb_{0.1}O_2$ (Figure S5, Supporting Information), attributed to the preferential segregation of Ir. This results in a structure referred to as a supported solid solution ($Sn_{0.9}Sb_{0.1}O_2$-supported 51-ISS) with high support-catalyst interaction, indicating that the 51-ISS has reached the critical dissolution limit of Ir in $Sn_{0.9}Sb_{0.1}O_2$.

It is worth noting that further optimization of synthesis parameters, such as the precursor composition, precursor to dispersion oxidant ratio, particle residence time, and shroud gas flow rates, could help reduce Ir phase separation and promote a more homogenous solid solution and higher valent Ir species. A strategy utilizing varying dispersion oxidant-to-fuel precursor feed ratios has been demonstrated as a key synthesis parameter for fine-tuning the particle size, specific surface area, Ir oxidation state, phase separation, and consequently catalytic activity. For instance, reducing the dispersion oxidant gas from 8 to 2 L min^{-1} per 5 mL min^{-1} of precursor feed resulted in a substantial reduction in the pure Ir phase. Furthermore, in an additional quenching experiment, 51-ISS-Q, where the cooling rate of the flame aerosol was increased by introducing 60 L min^{-1} of air at the flame tip to halt further catalyst evolution downstream of the flame,[39] a noticeable enhancement in OER performance was observed. A detailed discussion on these fundamental catalyst particle optimization mechanisms is provided in the supplementary information (Figures S6 and S8, Supporting Information and related content).

In a recent study by Doo et al.,[13] it was demonstrated that a polycrystalline catalyst with a low work function (WF), which closely matches the oxidized surface of the Ti porous transport layer (PTL), is essential for efficient charge transport at the catalyst layer (CL)/PTL interface in PEMWE systems. Specifically, at low catalyst loadings, the presence of amorphous phases in a catalyst was identified as a critical factor influencing band bending.[13] To evaluate the work function of the FSP-made 51-ISS, a comparison was made with commercial rutile-IrO_2 (Figure 2f). The small difference of ≈0.15 eV between 51-ISS (WF 4.53 eV) and IrO_2 (WF 4.38 eV) suggests a reduced transport barrier, indicating compatibility of the flame-derived catalyst for low-loaded PEMWE using the Ti (theoretical WF 4.33 eV) PTL (Figure 2g). The findings imply that the catalysts are largely crystalline rather than amorphous, despite the lack of clarity from the XRD analysis due to the small primary particle or nanocrystalline size of the materials.

Cyclic voltammetry (CV) and linear sweep voltammetry (LSV) techniques were employed to investigate the catalytic properties

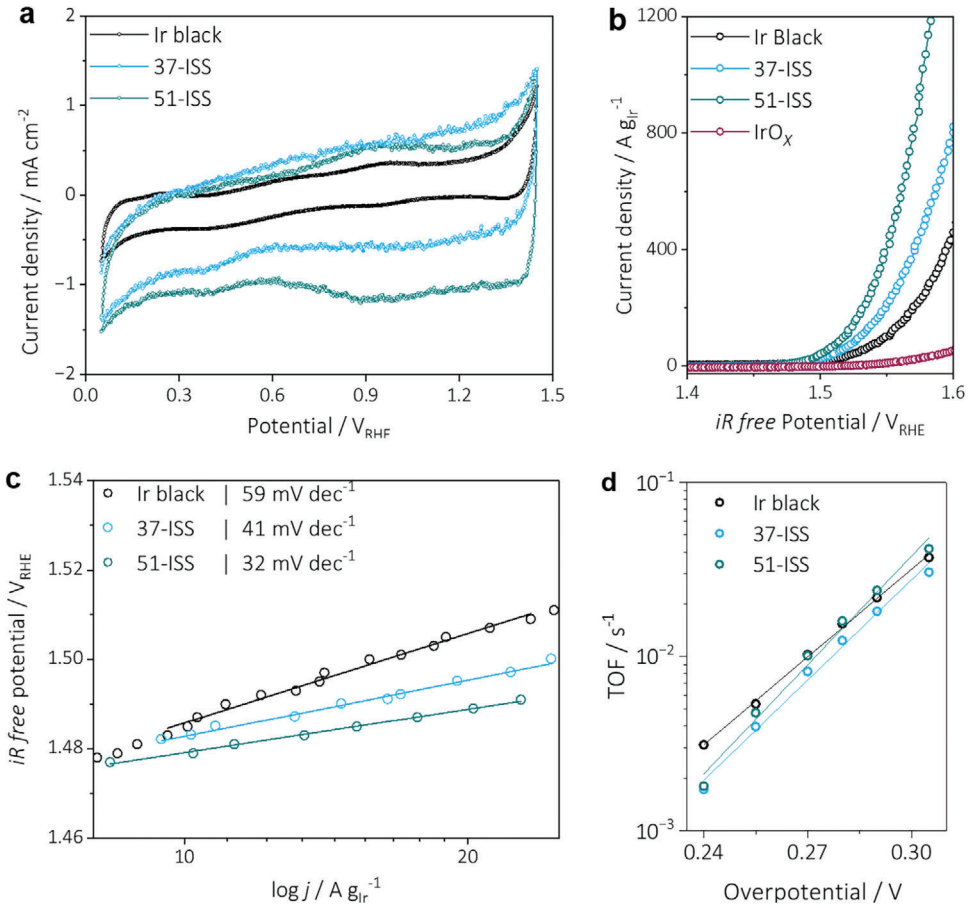

Figure 3. RDE measurements of FSP-made 37-ISS and 51-ISS compared with commercial Ir black: a) Cyclic voltammogram. b) Ir-mass specific OER activity plot. Additionally, FSP-made IrO_x (85 wt.% Ir) was included. c) Ir-mass-normalized Tafel plot. d) Turnover frequency (TOF) of Ir-black, 51-ISS, and 37-ISS for OER in acid at different overpotentials, related to the O_2 production per Ir site.

of the flame-made electrocatalysts and to compare them with commercial Ir black. After preconditioning steps, the CV results (**Figure** 3a) indicated that Ir black exhibited a prominent peak in the hydrogen adsorption region on metallic Ir (<0.35 V vs. reversible hydrogen electrode (RHE)), compared to 37-ISS and 51-ISS. The hydrogen adsorption–desorption peaks diminished rapidly as the metallic Ir surface oxidized. In both the first and tenth cycles, the voltammograms of the FSP catalysts essentially remained unchanged (Figure S9a, Supporting Information), unlike Ir black, which underwent an irreversible transformation of metallic Ir to hydrous oxide phases.[40] In the oxide formation region, a distinct redox couple[41] (Ir $(OH)_3$/Ir$(OH)_4$) was observed at ≈0.96 V vs. RHE for both Ir black and 51-ISS. This confirms the presence of a small percentage of metallic Ir,[42,43] or similar surface species in 51-ISS, as evidenced by the appearance of a cathodic peak in the first cycle at 0.4 V vs. RHE.[44] However, this peak was negligible for 37-ISS. The double layer charges associated with 51-ISS were higher than those for 37-ISS, suggesting a higher surface area and the presence of more active sites within the catalyst. Moreover, the double layer charges were significantly higher for both 51-ISS and 37-ISS compared to IrO_2. Consequently, the FSP method can produced catalysts with higher particle roughness.

The ohmic drop (iR)-corrected mass-normalized OER polarization curves (Figure 3b; Figure S10a, Supporting Information) reveal that both 31-ISS and 51-ISS outperformed the Ir black benchmark across the entire potential. For example, the overpotential required to reach 10 A g^{-1} for 51-ISS and 37-ISS, both with smaller primary particles ≈6 nm, was 7 and 2.5 mV less than that for Ir black, respectively. Further reducing the Ir content to 20 wt.%, the FSP-made 22-ISS still demonstrated performance comparable to Ir black (Figure S10a, Supporting Information). In contrast, the FSP-produced IrO_x (85 wt.% Ir) with primary particles up to 130 nm exhibited poor performance (Figure 3b; Figure S10, Supporting Information), as anticipated, underscoring the critical role of Sn and Sb in the structure. Consequently, IrO_x was not considered for further investigation.

Another commonly used metric to benchmark OER activity is the potential at a current density of 10 mA cm^{-2}, normalized to the geometric area of the electrode (Figure S11a, Supporting Information). In this context, 51-ISS again outperformed the Ir black, achieved 10 mA cm^{-2} at 1.52 V, comparable to values reported for high-performing Ir-mixed oxides.[9] Furthermore, at higher potentials, 51-ISS exhibited a mass-normalized current density four times higher than that of Ir black. The comparable performance of 37-ISS, containing only 35 wt.% Ir, to Ir black can

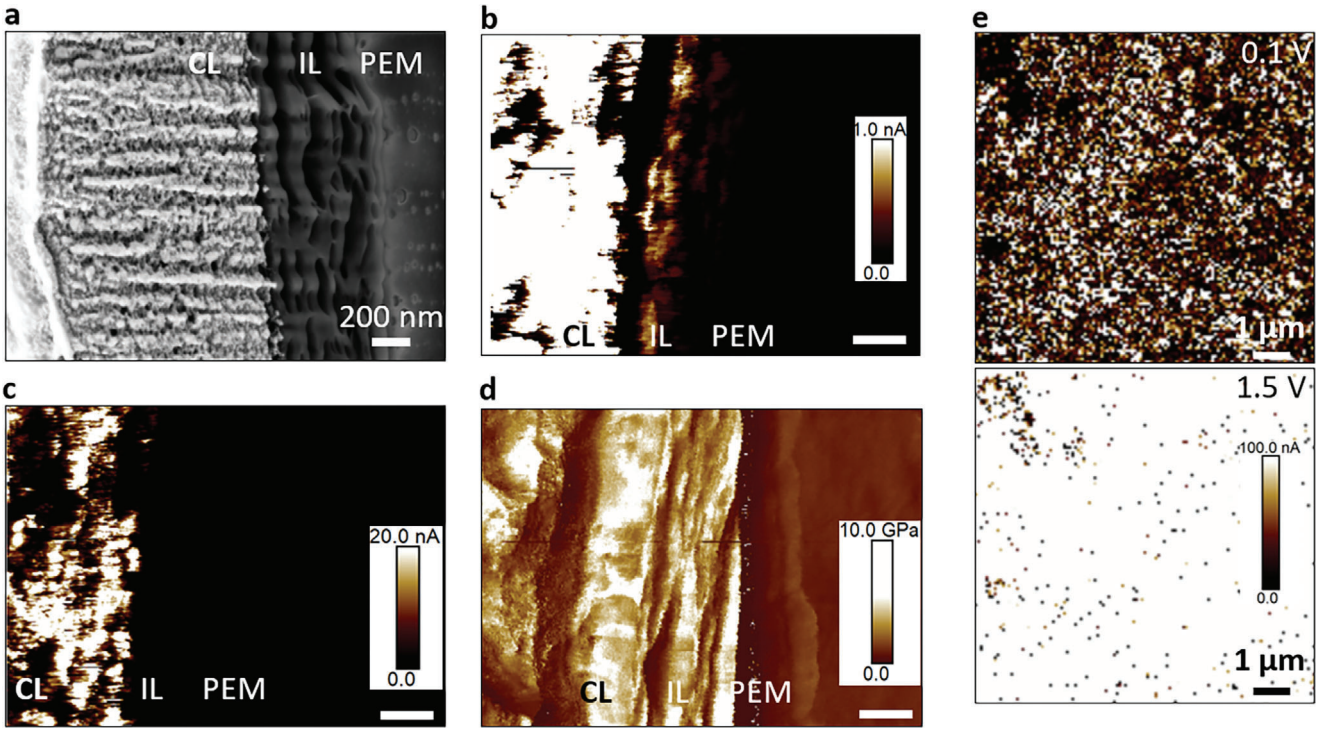

Figure 4. Microscopic analysis on a pristine 51-ISS-based CCM with 0.2 mg cm^{-2} of Ir loading on an IL coated PEM. a) representative SEM image at the anode CL-IL-PEM cross-section. b,c) AFM images in contact current mode at the anode CL-IL-PEM cross-section with corresponding d) Derjaguin–Muller–Toporov (DMT) modulus related to rigidity of the material. Scale bar: 200 nm. e) AFM current measurement on the anode CL surface. IV curve measurement between 0 and 2 V was performed. Representative image of average current response at 0.1 V (top) and 1.5 V (bottom) given.

be attributed to the efficient dispersion of Ir, which exposes more active sites. The exceptional OER performance of the 51-ISS may be attributed to the high availability of active Ir sites resulting from the presence of oxygen vacancies in the vicinity of Ir^{4+}.

The *i*R-free mass-normalized Tafel slopes (Figure 3c) were in the order of Ir black > 37-ISS > 51-ISS. The solid solutions exhibited slightly lower Tafel slopes (32–41 mV dec^{-1}) compared to those reported in recent publications[9] for high-performing catalysts. These slopes fell within the reported range (35–55 mV dec^{-1}) for Ir-based catalysts, indicating that the FSP-synthesized catalysts share similar mechanistic behaviors and rate-determining steps as Ir black, but with enhanced OER kinetics. Similar observations were more evident in the Ir-mass-normalized Tafel plot (Figure S11b, Supporting Information). Additionally, OER performance of the Ir black and 51-ISS was evaluated at the pH range of 0–1 to investigate the catalytic mechanism (Figure S11c, Supporting Information). Both catalysts exhibited strong pH dependent catalytic activity, suggest a proton coupled electron transfer (CPET) process.[45]

To gain more information about the intrinsic properties, the turnover frequency (TOF) was determined from the redox surface sites Ir^{III}/Ir^{IV} (Figure 3d; Table S2, Supporting Information) for 37-ISS and 51-ISS, and compared with Ir black.[46] Although the number of active sites per gram of Ir is relatively higher for 51-ISS, the TOF at lower overpotentials (<240 mV) is lower compared to Ir black. This indicates that the surface is covered with a range of catalytic sites, with the activity is dominated by the most active sites.[47] At higher overpotentials (>260 mV), 51-ISS reaches comparable or even higher TOF values than Ir black, suggesting a higher rate of increase in molar specific activity and possible activation of sites that are inactive at the lower overpotentials.

Chronopotentiometry tests performed at 10 mA cm^{-2} for 8 h showed no substantial failure of the catalyst activity (Figure S9b, Supporting Information). However, to gain a more accurate understanding of the catalyst's stability, long-term durability measurements under PEMWE operation conditions, compared with reference catalysts, are necessary.

The selected anode catalyst, 51-ISS, with the higher OER activity and lower metallic Ir content than IrO_x, IrO_2, and Ir black, was employed to fabricate the CCM for a 2000 h durability test in the PEMWE cell. The anode side catalyst layer (CL) had a controlled Ir loading of (0.20 ± 0.02) mg cm^{-2} (see materials and Experimental Section) and an average thickness of (0.9 ± 0.3) µm (**Figure 4a**), resulting in an Ir packing density of ≈2.2 g cm^{-3}. The thickness of the CL is influenced by the layer coating and drying techniques employed.[48] The suspension-based wet spray coating method utilized in this study tends to produce thinner CLs compared to dry or paste-based coating methods.[48] To improve the mechanical integrity of the CL, an interlayer (IL) consisting of graphene oxide (GO) with a loading of 0.03–0.04 mg cm^{-2} (≈0.0000022 mol cm^{-2} of carbon) was introduced between the PEM (Nafion 117) and the anode CL (see materials and methods section). The IL had a thickness of 0.4 µm (Figure 4a). It is known that use of carbon-based materials in a strong oxidative environment pose risk of degradation. Although the potential decrease at the

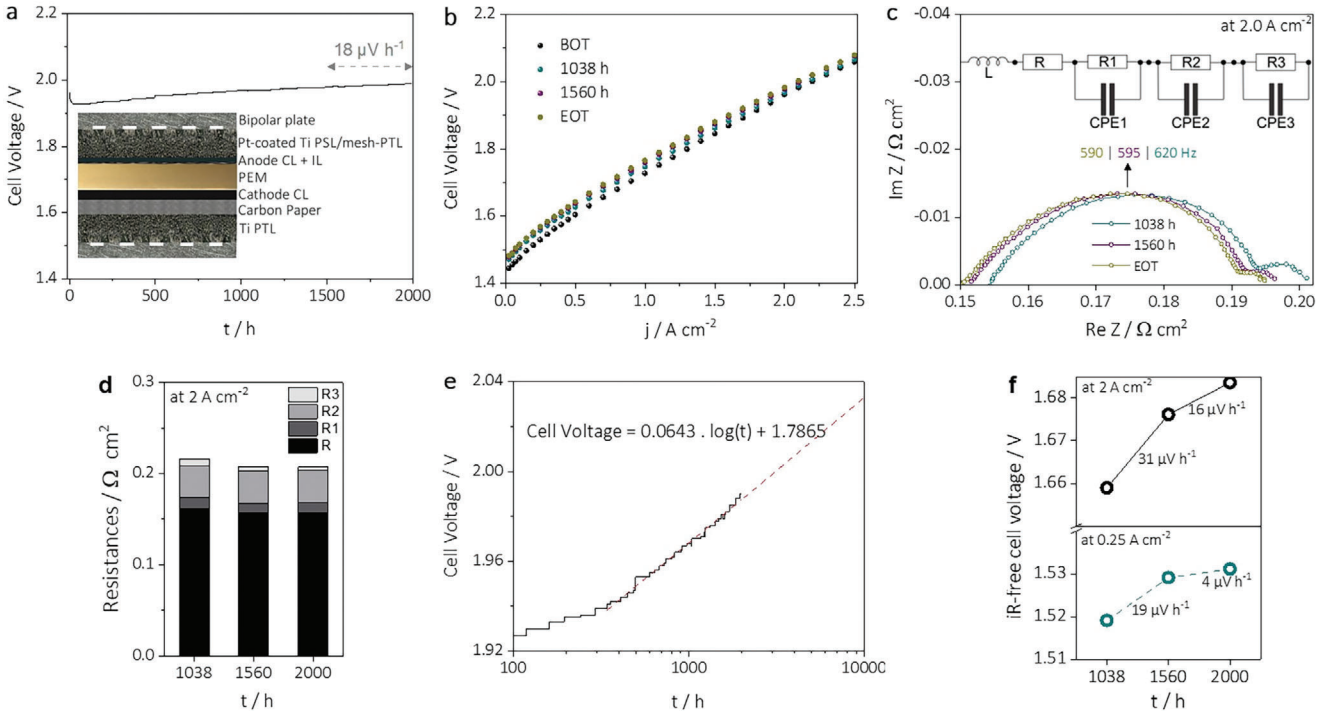

Figure 5. a) Durability test: 2 000 h durability test for 51-ISS in the PEMWE cell. Inset: Scheme of the PEMWE cell setup used. b) The evolution of the PEMWE cell voltage relative to the current density at different stages of the test, recorded up to 2.5 A cm^{-2} following the JRC EU-harmonized polarization protocol. Polarization curves were recorded without shut-down events and repeated twice, with only the second set of polarization curves shown here. c) electrochemical impedance spectroscopy (EIS) Nyquist plot of the cell resistance after 1038, 1560, and EOT at 2 A cm^{-2}. EIS were not measured at the BOT. Inset: corresponding equivalent circuit. R referred to ohmic. R1 referred to the hydrogen evolution reaction (HER), charge transfer resistance accompanied with double layer effects in the electrode, or the first charge transfer of the two-electron process of the OER. R2 referred to the charge transfer of the rate-determining step of the OER. R3 referred to the mass transport losses. CPE refers to constant phase element. d) deconvoluted resistances derived from Nyquist plot at 2 A cm^{-2} using the equivalent circuit from panel c. e) Cell voltage versus the logarithmic of time plot for the 2000 h durability test in the PEMWE cell. f) iR-free cell voltage at 0.25 and 2 A cm^{-2}.

PEM-CL interphase is expected to reduce the oxidizing environment compared to the CL surface,[49] to protect the GO from corrosion the ionomer to GO weight ratio of 2 was used in the IL. This ratio ensures that the GO fully covered by the ionomer, similar to a sandwiched layer between two Nafion membranes.[50] The thickness of the CL is comparable to IrO_2/TiO_2-based CL,[6] but with smaller particles sizes (4 ± 2) nm. This is possible because flame-made catalyst particles form contiguous structures (Figure 1c; Figure S1, Supporting Information) with meso and macro pores between primary particles. These pores can also reduce tortuosity and assist mass-transport. It is anticipated that the ionomer in the CL partially evaporates during the sample preparation via focused ion-beam (FIB) milling, leaving pores. Therefore, distinguishing between these pores and those that originally existed in the CL can be challenging. However, the ionomer distribution in the CL was verified from nano-electrical-mechanical atomic force microscopy (AFM) measurements at the PEM-IL-CL cross-section using Pt-coated tip (diameter 10 nm) in PeakForce-TUNA mode (Figure 4b,c). The anode layer exhibited an electrically conductive area fraction of >50% at a bias of 1 V (Figure 4c), with the remaining area being non-conductive or less-conductive, majorly covered with ionomer and pores. This indicates a highly homogeneous and well-interconnected distribution of catalyst and ionomer, even with a low Ir loading of 0.2 mg cm^{-2}. This finding contradicts the common assumption that low-loaded thin CLs are inherently inhomogeneous.[6] A closer examination of Figure 4b,c reveals that while the IL has low electronic conductivity, it possesses rigidity (Figure 4d) comparable to the CL. Therefore, it can be inferred that the IL does not significant contribute to the catalytic reactions (a finding corroborated by the RDE measurements, Figure S12, Supporting Information), but it can help in maintaining mechanical integrity of the interphase.

The AFM results of i(V) mappings (Figure 4e) suggest that the contact resistance between the CL and any Pt-coated surfaces – such as the microporous layer (MPL), porous sintered layer (PSL) and felt – is negligible at a 1.5 V bias. This is supported by the observed ohmic behavior across numerous measured points. Therefore, if present, any inter-particles grain boundary resistance due to the higher specific surface area of the catalyst network could be the predominant factor affecting performance.

The PEMWE cell (**Figure** 5a inset) measurements were conducted at 80 °C and ambient pressure. A 2000 h durability test was performed at constant current density of 2 A cm^{-2} (Figure 5a), with intermediate shutdowns at 1038 h and 1560 h, in addition to the beginning-of-test (BOT) and end-of-test (EOT) characterizations. The test was interrupted (Figure S13, Supporting Information) once for test bench maintenance at ≈500 h and

twice for the diagnostic tests. A polarization curve at the BOT recorded after 2 h of constant operation reached 2.0 A cm^{-2} at 1.961 V (Figure 5b; Figure S14, Supporting Information) and 89 mg_{Ir} kW^{-1} at a cell voltage efficiency of 70%$_{LHV}$. This performance is relatively high compared to recent literature on PEMWE using even higher Ir loadings (0.25–0.30 mg cm^{-2}) with N117 and N212 membranes (Figure S15, Supporting Information).[34,51–53] A detailed discussion on literature comparison of performance and durability is provided in the supplementary information (Tables S3 and S4 and Figures S15 and S16, Supporting Information, and related content). Furthermore, it surpasses the 2030 target (250 mg kW^{-1}) of Clean Hydrogen Joint Undertaking for the use of critical raw materials as catalysts in PEMWE.[54] The nearly linear cell voltage and flat *i*R-free cell voltage profiles at higher current densities (>1 A cm^{-2}) indicate a negligible combined impact from kinetics and mass-transport losses, with a constant ohmic resistance. The evolution of cell voltage from BOT, 1038 to 1560 h (Figure 5b) shows that performance decay over time is less pronounced at higher current densities (> 0.5 A cm^{-2}) compared to lower current densities (< 0.5 A cm^{-2}) due to a higher high frequency resistance (HFR) drop at higher current densities (Figure 5c,d; Figure S18, Supporting Information). However, it is evident from Figure 5d that although the rate of HFR drop decreases over time, the rate of performance decay continues to decline (Figure 5a) and reaches 18 μV h^{-1} during the last 500 h of operation, down from 21 and 24 μV h^{-1} during the last 1000 and 1500 h of operation, respectively. While the average decay rate for the entire 2000 h test duration is 14 μV h^{-1}. These degradation rates are comparable to those reported by Zeng et al.[34] and Mirshekari et al.,[53] where IrO_x was produced and sprayed (≤0.3 mg_{Ir} cm^{-2}) in one step using the reactive spray deposition technique, albeit their durability tests were conducted at 50 °C and 1.8 A cm^{-2}. Moreover, these degradation rates are about two to three times lower than the degradation rates observed for commercial IrO_2 for 1209 h and Ir black for 500 h (Figure S17 and Table S5, Supporting Information) tested using the same PEMWE cell set up with controlled Ir loading of 0.2 mg cm^{-2}. The performance decay for commercial IrO_2 during the last 500 and 1000 h of operation is ≈34 and 32 μV h^{-1}, respectively, compared to 18 and 21 μV h^{-1} for 51-ISS. For commercial Ir black, the performance decay rate between 100 and 500 h is ≈41 μV h^{-1}.

Additionally, the decreasing in decay rate with increasing test duration suggests that over the long run (several thousand hours), the rate of cell voltage decay may potentially further reduce upon stabilization. However, a durability test much longer than 2000 h, which is unfortunately impractical, is required to validate this phenomenon. The relationship between cell voltage and the logarithm of time shows a strong linear correlation from 300 to 2000 h (Figure 5e), allowing for the projection of the decay rate over approximately another decade of time through extrapolation. For example, the projected decay rate between 9000 and 10 000 h is <3 μV h^{-1}. Furthermore, to understand the catalyst stability over the long run, iR-free cell voltage at 0.25 A cm^{-2} (kinetic dominant current) versus logarithm of time was also plotted (Figure S19, Supporting Information). The extrapolated results also show a linear relationship and indicate a decreasing trend in the rate of catalyst activity decay.

As seen in Figure 5a, the cell voltage initially drops from 1.961 to 1.927 V over the first 29 h of the operation, after which it stabilizes at 1.927 V for 89 h before it begins to rise. This pattern of behavior aligns with observations by Retuerto et al., and Torrero et al.[9,55] This phenomenon may be attributed to a trade-off between catalyst activation and cell degradation, potentially caused by reorganization of catalyst-ionomer (to be discussed later). Initially, the catalyst activation predominates, enhancing performance and resulting in a voltage drop. Subsequently, both catalyst activation and cell degradation compensate for each other, maintaining the cell voltage stability for 89 h before the activation process ceases leading to the observed increase in cell voltage.

It is important to note that the above rates of cell voltage decay were estimated from Figure 5a and not from the polarization curves (Figure 5b), where possible recovery of reversible performance loss during dynamic measurement conditions displayed a cell voltage decay of 11 μV h^{-1} between 1560 and 2 000 h. Furthermore, the *i*R-free cell voltage decay (Figure 5f) at 0.25 A cm^{-2} (kinetic dominant) and 2 A cm^{-2} (mass-transport dominant) – regions more appropriate[52] for understanding the catalyst and CL stability by eliminating the ohmic contributions – also continue to decrease, reaching 4 and 16 μV h^{-1}, respectively, between 1560 and 2000 h. Möckl et al.[52] reported such a polarization curve-based (*i*R-free) cell voltage decays and observed a major decrease in the rate of cell voltage decay with prolonged test duration from 1000 to 3700 h for supported iridium catalysts.

SEM image of the anode-side of the CCM operated for 2000 h (**Figure 6a**) reveals noticeable changes in the CL compared to the pristine CCM (Figure 4a). While a direct comparison of thickness of spray-deposited thin CLs is challenging, SEM analysis revealed an increase in packing density at several observation points. Notably, the mechanical integrity of CL and PEM, interphases between CL-IL-PEM, and thickness of PEM remained largely preserved. Interestingly, the IL structure (ionomer-covered GO) showed no visible sign for corrosion even after the 2 000 h stability test at 2 A cm^{-2} (amount to 149.2 mol cm^{-2} of e^-) and maintained excellent contact with both the PEM and CL. Otherwise, 0.000003% (two-electron carbon corrosion) or 0.000006% (four-electron carbon corrosion) of the total electrons could have removed 0.000022 mol cm^{-2} of carbon (as GO), implies that the Faradaic efficiency of carbon corrosion is negligible. This validates the safe deployment of a thin ionomer-covered GO layer at the PEM-CL interphase.

Examination of elemental compositions on both the surface and the cross section of the operated anode CL compared to the pristine CL (Figure S20, Supporting Information) revealed an increase in the relative weight fraction of Sn and Sb as compared to Ir, in contrary to the common belief that Sn and Sb are prone to dissolution during the operation. For closure examination of the operated CCM, a small amount of powder collected from the anode CL by scratching and was analyzed using High resolution (HR)-TEM (Figure 6b). The nanoparticles covered with ionomer found to have uniformity in size and maintained crystallinity alike pristine nanoparticles. The elemental maps with EDX (Figure S21, Supporting Information) showed the ratio of Ir to Sn+Sb counts at any given point within the 50 × 50 nm^2 area likely unchanged, indicating the ability of the 51-ISS to retain the nanometer scale mixing of all three elements without noticeable phase separation during the OER process for 2000 h.

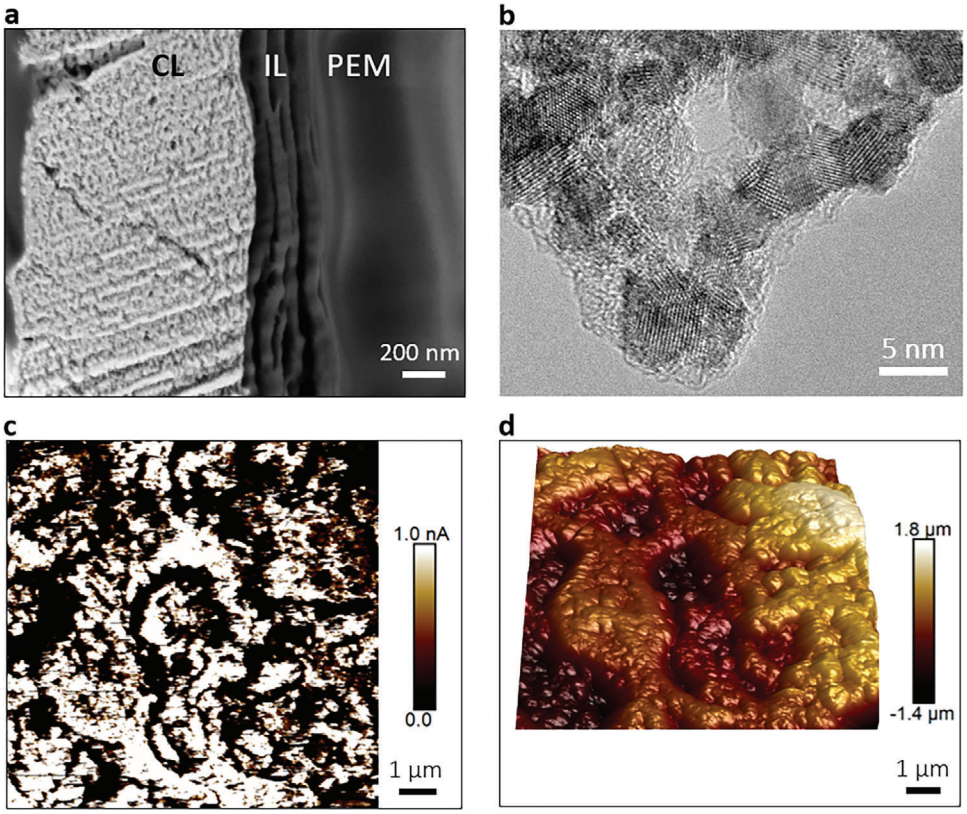

Figure 6. Post-durability characterizations for the 2 000 h tested CCM: a) representative SEM image at the anode CL-IL-PEM interphase. b) representative HR-TEM image of the anode catalyst. c) AFM PeakForce Tapping-mode electronic conductivity measurement on the anode CL and d) the corresponding height measurement.

In the absence of noticeable precipitation of Ir, Sn, or Sb in the IL and PEM, further detailed investigation is required to elucidate the cause and rate of changes in the CL composition. Although physical loss of catalyst from CL is common in electrolysis,[34,55] we propose that testing the CCMs after varying operational durations and analyzing trace metals concentration in operated water at different stages would be beneficial.

AFM measurements were performed to compare the surface morphology and electronic properties of the CL before (Figure S22, Supporting Information) and after (Figure 6c,d) 2000 h of operation. After operation, a less than 10% increase in the conductive area was observed (Figure 6c), potentially indicating ionomer degradation or reorganization during the cell operation, particularly during the break-in procedure.[56] The roughness of the CL decreased by ≈10% (Figure 6d; Figure S22b, Supporting Information), suggesting a reduction in micro-porosity and thus an increased mass transport resistance. This observation contrasts with the results from the EIS plots (Figure 5c). The AFM images reveal that the overall morphology, electronically conductive area, and maximum roughness of the CL remained largely unchanged after operation, indicating no severe degradation at a large-scale. The observed changes in roughness may be attributed to contact with the PTL rather than a decrease in micro-porosity. Nevertheless, the overall performance and durability of the PEMWE with FSP-made 51-ISS anode catalyst is comparable to, or even higher, that of commercial CCMs with ten times higher Ir loading.[34,52,57] Thus, the 51-ISS, catalyst produced via FSP has the potential to be integrated into large area stacks of the commercial PEMWE systems. It has been demonstrated that up to 500 g h^{-1} of material can be produce by FSP,[29] with existing pilot plants already operational.[58] At this rate, continuous operation over 330 days per year could yield ≈4 t of annual production of the 51-ISS catalyst for PEMWE, potentially meeting global green H_2 demand.

3. Conclusion and Outlook

Aiming for low Ir content PEMWE and cost-efficient production of high-performance catalysts, we have developed self-preserved nanocrystalline solid solution catalysts of $Ir_{\gamma}Sn_{0.9(1-\gamma)}Sb_{0.1(1-\gamma)}O_x$ (γ = 0.37, 0.51, respectively) that hold immiscible elements in a single process step using rapid and scalable FSP techniques. These materials, with highly dispersed Ir nanoparticles (≈4 nm) having non-noble metal neighbors and abundant oxygen defects, exhibit high activity and stability toward OER. A homogeneous conductive CL utilizing the flame-derived catalysts displayed high performance and exceptional durability over 2000-h with only 18 µV h^{-1} degradation rate at a nominal current density of 2 A cm^{-2} in PEMWE with a low Ir loading of 0.2 mg cm^{-2}. This demonstrates the potential of the FSP-made catalyst to enable rapid com-

mercialization of PEMWE, without the need for numerous stages of scale-up in catalyst production.

The findings presented in this study underscore the potential of high-temperature flame with a steep thermal gradient to stabilize thermodynamically unstable solid solutions. By employing Ir-Sn-Sb-based solid solutions, it is possible to fabricate a porous, rigid, and electrically contiguous CL even with low Ir loading. The combination of low work function and size-dependent surface-enriched Ir dispersion of these FSP-derived materials suggest possibilities for further compositional exploration, positioning them as promising candidates for ultra-low Ir-loaded PEMWE. The results are also encouraging for the development of more challenging electrocatalysts, such as high entropy electrocatalysts and highly dispersed supported single-atom catalysts at high synthesis rates.

4. Experimental Section

Physicochemical Characterization: The phase characteristics of the as-synthesized samples were investigated using X-ray diffractometers from Bruker D8. To ensure flat surface and minimizing air scattering, the samples were ground prior to analysis. A low background holder with a small powder volume was used, and the samples were scanned between diffraction angles 5–90° using a 1D detector. Crystallite size for each catalyst was determined from XRD data using the Debye–Scherrer equation. Morphology and semi-quantitative elemental composition of the as-synthesized powders and CCMs were analyzed using a Zeiss Crossbeam 350 scanning electron microscope equipped for energy dispersive spectroscopy (Oxford instruments) at an acceleration voltage of 2–5 kV and working distance of 5 mm. The samples from CCMs were prepared by argon ion cutting using a Jeol IB-19520CCP at 6 kV and room temperature. For section of the CL FIB-SEM was used at an angle of 54° while correcting the angle for the thickness measurements. The cuts were performed with 3 nA FIB current at 30 V for the coarse trench, and the final surface was prepared using a 700 pA current for the FIB at 30 V. Transmission electron microscopy (TEM) analysis was performed using and JEOL JEM-F2100 and JEOL JEM-ARM200F machines, the latter is equipped with a Schottky emitter and Cs-probe corrector, both operated at 200 kV. The EDS analysis was by both microscopes, while HAADF imaging was done using JEOL TEM ARM200F with a semi convergence angle of 25 mrad s. Particle size for each catalyst was determined from TEM or SEM images by averaging at least 50 to up to 200 individual particles. Chemical analyses via XPS were performed using monochromated Al Kα radiation with an energy of 1486.74 eV on a spectrometer with a hemispherical electron analyzer and a base pressure of 2×10^{-10} mbar (ThermoScientific / FEI ESCALAB Xi$^+$). Signal processing involved the use of convoluted Gaussian / Lorentzian peak profiles and the application of a Shirley background.[59] Valence band spectra and work function measurements were conducted on the same system using He I radiation (21.22 eV). A bias voltage of −10 V applied to the sample for the work functions measurements. XANES spectra were measured on an easyXAFS 300+ X-ray absorption spectrometer at the Ir L3 edge (11.215 keV, 3.7 eV resolution) using an X-ray source with a Mo anode operating at 30 kV and 26 mA and a Si(911) spherically bent channel-cut monochromator. Samples were prepared by diluting 15–20 mg of sample (depending on the Ir content of each sample) in methyl cellulose to a total weight of 40 mg and pressed into 13 mm pellets of uniform thickness at 10 tons and sealed in Kapton tape. Spectra were collected using a KETEK AXAS-M silicon drift detector with an exposure time for each data point of 3s. Spectra are the total of 10 scans. The energy of all spectra was corrected by a scalar factor to match the known edge position of Ir metal. The data were analyzed using the Athena program of the Demeter software package.[60] The intensities of the white line peaks of the normalized data were fitted to a pseudo-Voigt function (gave the best agreement to the data) with the edge jump being modeled by an arctan function (Figure S3, Supporting Information).

Half-Cell OER Testing: CV and LSV measurements of the catalysts were performed in a standard three-electrode electrochemical cell using a rotating disk setup (RRDE-3A, BAS Inc, Japan). The measurements were conducted at room temperature in an argon-purged 0.5 M H_2SO_4 electrolyte, expect that the pH dependent RDE measurements were conducted in $HClO_4$. A Pt wire and a reversible hydrogen electrode (RHE) (GASKATEL) served as the counter and reference electrodes, respectively. The working electrode was a catalyst-coated glassy carbon electrode (0.1256 cm^2). Electrochemical measurements were performed using an Interface 5000E potentiostat/galvanostat (GAMRY instruments). Catalyst ink was prepared by dispersing as-synthesized catalyst powders in a mixture of isopropyl alcohol and ultra-pure water (1:3 v/v), into which desired amount of Nafion solution (5 wt.%) was added to achieve an ionomer to catalyst weight ratio of 0.2. The dispersion was then sonicated for 30 min and pipetted onto the surface of a glassy carbon electrode (GCE) to achieve 70 µg cm^{-2} of Ir loading. The potential was swept between 0.05 and 1.45 V (vs. RHE) for 10 cycles at a scan rate of 50 mV s^{-1} under electrode rotation of 2500 rpm to oxidize the surface supported Iridium nanoparticles. The electrochemical OER catalytic activity was recorded by linearly sweeping the voltage between 1.2 and 1.7 V (vs. RHE) at 10 mV s^{-1} for 5 cycles. All LSVs were corrected for ohmic resistances in situ within the potentiostat framework. To ensure reliability of the catalyst performance, all the developed catalysts were tested at least thrice in the RDE set up (Figure S23, Supporting Information) and compared with Ir black. For TOF calculation, the active surface redox sites were determined by integrating the anodic oxidation peak of Ir^{III} to Ir^{IV} without the capacitive current.[46]

AFM Measurements: Anode surface and PEM-IL-CL interface AFM measurements were performed on a pristine CCM. A piece of 5 × 5 mm^2 sample was cut using a razor blade and attached to a steel disc covered with conductive carbon tape. An additional piece of conductive tape was placed on the top corner of the sample to facilitate electrical contact. The measurements were conducted using a Bruker ICON XR AFM. For CL surface, the current over a bias window between 0 and 2 V ((i)V curve) was mapped using DCUBE-TUNA mode, while the bias was ramped over the specific hold time of 0.1 s for each sample point (128 × 128 points) on a 100 µm^2 area. For interfacial cross-section measurement between PEM and CL, Bruker PF-TUNA mode was employed with NCH-PPT tips (Nanosensors) using a PeakForce of 100 nN and an amplitude of 150 nm at 0.488 Hz. The CCM cross-section was prepared using a Leica microtome (Leica Autocut) while the CCM was sandwiched between two polystyrene sheets (no embedding). The peak current (current at maximum force) was used for evaluation. PeakForce Tapping electronic current AFM measurements (PeakForce TUNA) were performed to compare the catalyst layer surface morphology and electronic behavior of a CCM before and after 2000 h of operation.

CCM Preparation: The catalyst inks were prepared by dispersing electrocatalyst powder in a solvent mixture of water and isopropanol (1:1 volumetric ratio) and ionomer solution (Nafion D521) using an ultrasonic homogenizer for 30 min at 25 °C. The final ink concentration was 1.0 mg of catalyst powder per ml of ink. Nafion 117 membrane (≈183 µm) was used as PEM. The FSP-made as-synthesized $Ir_{0.51}Sn_{0.44}Sb_{0.05}O_2$ and as-received commercial Pt/C (HiSPEC4000) were used as the anode and cathode catalysts, respectively. In-house optimized wet spray coating technique was used for catalyst deposition onto the PEM at 90 °C. The ink composition was optimized in order to achieve CCMs with Ir and Pt loadings of (0.20 ± 0.02) and (0.40 ± 0.02) mg cm^{-2} in the anode and cathode layers, respectively, and ionomer content of 17 and 23 wt.% in the anode and cathode layers, respectively (high cathode side Pt loading was used to minimize the impact of the HER kinetics on the cell performance). An IL was used between PEM and anode CL in order to maintain structural stability of the anode CL. The IL ink composition was optimized to achieve a graphene oxide loading of 0.03–0.04 mg cm^{-2} and ionomer content of 55 wt.% in the IL. The prepared CCMs were then hot pressed at 5 MPa and 125 °C for 10 min.

PEMWE Testing: As shown in the inset of the Figure 5a, a Ti porous sintered layer (PSL) on Ti mesh (PSL/mesh-PTL) compound PTL coated with Pt[55] was deployed in contact with anode CL, and a carbon paper (Spectracarb 2050A-1050) was deployed in contact with cathode CL. Ti-

BPPs were employed on both sides. The active area of the cell was 4 cm^{-2}. A compression force of 2 N m was applied throughout the tests. Distilled water (18 MΩ cm^{-1}) flow rates in the anode and cathode compartments were maintained at 3 L h^{-1}. All the electrochemical tests were conducted at 80 °C and ambient pressure. 2000 h durability test in constant current mode at 2 A cm^{-2} was performed using a power supply (EA-PSE 9040–510) from Elektro-Automatik. The JRC EU-harmonized protocol[61] with a dwell time of 60 s per current step was followed for the polarization curve measurement using the same power supply. Polarization curves were recorded without shut-down events and repeated twice. Only the second polarization curves were used for analysis and shown in Figure 5b. The cell was then disconnected (shut-down) from power supply and connected with a potentiostat (Zahner IM6 and PP241) for electrochemical impedance spectroscopy (EIS) measurements between 0.1 Hz and 70 kHz. EIS were performed at different current densities (0.1, 0.25, 0.6, 1.0, and 2.0 A cm^{-2}), with an AC amplitude of 5% of the applied DC current. The HFR for calculating the *i*R-free PEMWE cell voltage was determined from the high frequency intercept of the real axis of the Nyquist EIS plot. EIS deconvolution of associated electrochemical processes was carried out based on our previous work.[62]

Supporting Information

Supporting Information is available from the Wiley Online Library or from the author.

Acknowledgements

The authors thank the staff of the DLR, Noriko Sata for support with XRD measurements.

Open access funding enabled and organized by Projekt DEAL.

Conflict of Interest

The authors declare no conflict of interest.

Author Contributions

S.V. performed conceptualization. K.A.F., P.G., A.S.G., and L.M. acquired funding acquisition. S.V., S.A., I.B., O.R., T.M., E.A., and D.P.E. performed investigation. S.V., J.M, A.S.G., K.W., P.G., and I.B. performed methodology. J.M, A.S.G., P.G., and K.A.F. performed supervision. S.V. wrote the original draft. All the authors wrote, reviewed, and edited the final manuscript. PEMWE cell utilizing commercial Ir black (Figure S16, Supporting Information) and IrO_2 (Figure S17, Supporting Information) was tested by S.A.

Data Availability Statement

The data that support the findings of this study are available from the corresponding author upon reasonable request.

Keywords

electrocatalysts, flame spray pyrolysis, low loading, durability, solid solution, water electrolysis

Received: April 11, 2024
Revised: September 20, 2024
Published online:

[1] European Commission, European Green Deal. https://climate.ec.europa.eu/eu-action/european-green-deal (accessed: October 2023).
[2] The white house, Inflation Reduction Act. https://www.whitehouse.gov/cleanenergy/clean-energy-tax-provisions/ (accessed: October 2023).
[3] D. Bohm, M. Beetz, M. Schuster, K. Peters, A. G. Hufnagel, M. Doblinger, B. Boller, T. Bein, D. Fattakhova-Rohlfing, *Adv. Funct. Mater.* **2020**, *30*, 2070001.
[4] Johnson Matthey, PGM Price Charts http://www.platinum.matthey.com/prices/price-charts (accessed: October 2023).
[5] M. A. Hubert, L. A. King, T. F. Jaramillo, *ACS Energy Lett.* **2022**, *7*, 17.
[6] M. Bernt, C. Schramm, J. Schroter, C. Gebauer, J. Byrknes, C. Eickes, H. A. Gasteiger, *J. Electrochem. Soc.* **2021**, *168*, 084513.
[7] V. A. Saveleva, L. Wang, O. Kasian, M. Batuk, J. Hadermann, J.-J. Gallet, F. Bournel, N. Alonso-Vante, G. Ozouf, C. Beauger, K. J. J. Mayrhofer, S. Cherevko, A. S. Gago, K. A. Friedrich, S. Zafeiratos, E. R. Savinova, *ACS Catal.* **2020**, *10*, 2508.
[8] L. C. Seitz, C. F. Dickens, K. Nishio, Y. Hikita, J. Montoya, A. Doyle, C. Kirk, A. Vojvodic, H. Y. Hwang, J. K. Norskov, T. F. Jaramillo, *Science* **2016**, *353*, 1011.
[9] L. P. María Retuerto, J. Torrero, M. A. Salam, Á. Tolosana-Moranchel, D. Gianolio, P. Ferrer, P. Kayser, V. Wilke, S. Stiber, V. Celorrio, M. Mokthar, D. G. Sanchez, A. S. Gago, K. A. Friedrich, M. A. Peña, J. A. Alonso, S. Rojas, *Nat. Commun.* **2022**, *13*, 7935.
[10] Y.-R Zheng, J. Vernieres, Z. Wang, K. Zhang, D. Hochfilzer, K. Krempl, T.-W. Liao, F. Presel, T. Altantzis, J. Fatermans, S. B. Scott, N. M. Secher, C. Moon, P. Liu, S. Bals, S. Van Aert, A. Cao, M. Anand, J. K. Nørskov, J. Kibsgaard, I. Chorkendorff, *Nat. Energy* **2022**, *7* , 55.
[11] Z. P. Shi, J. Li, J. D. Jiang, Y. B. Wang, X. Wang, Y. Li, L. T. Yang, Y. Y. Chu, J. S. Bai, J. H. Yang, J. Ni, Y. Wang, L. J. Zhang, Z. Jiang, C. P. Liu, J. J. Ge, W. Xing, *Angew. Chem., Int. Ed.* **2022**, *61*, 20221234.
[12] L. Moriau, M. Smiljanic, A. Loncar, N. Hodnik, *ChemCatChem* **2022**, *14*, 202200586.
[13] G. Doo, J. Park, J. Park, J. Heo, J. Jung, D. W. Lee, H. Bae, J. Hyun, E. Oh, J. Kwen, K. M. Kim, H.-T. Kim, *ACS Energy Lett.* **2023**, *8*, 2214.
[14] Y. N. Regmi, E. Tzanetopoulos, G. S. Zeng, X. Peng, D. I. Kushner, T. A. Kistler, L. A. King, N. Danilovic, *ACS Catal.* **2020**, *10*, 13125.
[15] H. Jin, B. Ruqia, Y. Park, H. J. Kim, H. S. Oh, S. I. Choi, K. Lee, *Adv. Energy Mater.* **2021**, *11*, 2003188.
[16] G. F. Li, H. M. Yu, D. L. Yang, J. Chi, X. Y. Wang, S. C. Sun, Z. G. Shao, B. L. Yi, *J. Power Sources* **2016**, *325*, 15.
[17] G. F. Li, H. M. Yu, X. Y. Wang, S. C. Sun, Y. K. Li, Z. G. Shao, B. L. Yi, *Phys. Chem. Chem. Phys.* **2013**, *15*, 2858.
[18] N. J. Perez-Viramontes, V. H. Collins-Martinez, I. L. Escalante-Garcia, J. R. Flores-Hernandez, M. Galvan-Valencia, S. M. Duron-Torres, *Catalysts* **2020**, *10*, 524.
[19] J. Kwon, S. Sun, S. Choi, K. Lee, S. Jo, K. Park, Y. K. Kim, H. B. Park, H. Y. Park, J. H. Jang, H. Han, U. Paik, T. Song, *Adv. Mater.* **2023**, *35*, 2300091.
[20] J. Edgington, N. Schweitzer, S. Alayoglu, L. C. Seitz, *J. Am. Chem. Soc.* **2021**, *143*, 9961.
[21] S. Q. Hu, S. Y. Ge, H. M. Liu, X. Kang, Q. M. Yu, B. L. Liu, *Adv. Funct. Mater.* **2022**, *32*, 202201726.
[22] J. Y. Xu, G. Y. Liu, J. L. Li, X. D. Wang, *Electrochim. Acta* **2012**, *59*, 105.
[23] H. N. Nong, T. Reier, H.-S. Oh, M. Gliech, P. Paciok, T. Ha, T. Vu, D. Teschner, M. Heggen, V. Petkov, R. Schlögl, T. Jones, P. Strasser, *Nat. Catal.* **2018**, *1*, 841.
[24] H. S. Oh, H. N. Nong, P. Strasser, *Adv. Funct. Mater.* **2015**, *25*, 1074.
[25] L. Mädler, H. K. Kammler, R. Mueller, S. E. Pratsinis, *J. Aerosol Sci.* **2002**, *33*, 369.

[26] C. D. Rosebrock, T. Wriedt, L. Mädler, K. Wegner, *AIChE J.* **2016**, *62*, 381.
[27] S. Venkatesan, J. Mitzel, K. Wegner, R. Costa, P. Gazdzicki, K. A. Friedrich, *Renewable Sustainable Energy Rev.* **2022**, *158*, 112080.
[28] R. Strobel, S. E. Pratsinis, *Phys. Chem. Chem. Phys.* **2011**, *13*, 9246.
[29] A. J. Gröhn, S. E. Pratsinis, A. Sanchez-Ferrer, R. Mezzenga, K. Wegner, *Ind. Eng. Chem. Res.* **2014**, *53*, 10734.
[30] C. L. McDaniel, S. J. Schneider, *J. Res. Natl. Bur. Stand. A Phys. Chem.* **1967**, *71A*, 119.
[31] Y. Yao, Z. Huang, P. Xie, S. D. Lacey, R. J. Jacob, H. Xie, F. Chen, A. Nie, T. Pu, M. Rehwoldt, D. Yu, M. R. Zachariah, C. Wang, R. Shahbazian-Yassar, J. Li, L. Hu, *Science* **2018**, *359*, 1489.
[32] D. Escalera-Lopez, S. Czioska, J. Geppert, A. Boubnov, P. Rose, E. Saraci, U. Krewer, J. D. Grunwaldt, S. Cherevko, *ACS Catal.* **2021**, *11*, 9300.
[33] J. M. Roller, M. J. Arellano-Jimenez, R. Jain, H. R. Yu, C. B. Carter, R. Maric, *J. Electrochem. Soc.* **2013**, *160*, F716.
[34] Z. Q. Zeng, R. Ouimet, L. Bonville, A. Niedzwiecki, C. Capuano, K. Ayers, A. P. Soleymani, J. Jankovic, H. R. Yu, R. Maric, S. Bliznakov, *J. Electrochem. Soc.* **2022**, *169*, 054536.
[35] C. L. McDaniel, S. J. Schneider, *J. Res. Natl. Bur. Stand. A Phys. Chem.* **1969**, *73A*, 213.
[36] E. Wiberg, A. F. Holleman *Inorg. Chem*, Elsevier, Amsterdam, The Netherlands **2001**.
[37] J. A. H. Dreyer, S. Pokhrel, J. Birkenstock, M. G. Hevia, M. Schowalter, A. Rosenauer, A. Urakawa, W. Y. Teoh, L. Mädler, *CrystEngComm* **2016**, *18*, 2046.
[38] C. Ye, J. Liu, Q. Zhang, X. Jin, Y. Zhao, Z. Pan, G. Chen, Y. Qiu, D. Ye, L. Gu, G. I. N. Waterhouse, L. Guo, S. Yang, *J. Am. Chem. Soc.* **2021**, *143*, 14169.
[39] K. Wegner, S. E. Pratsinis, *AIChE J.* **2003**, *49*, 1667.
[40] S. Cherevko, S. Geiger, O. Kasian, A. Mingers, K. J. J. Mayrhofer, *J. Electroanal. Chem.* **2016**, *773*, 69.
[41] P. G. Pickup, V. I. Birss, *J. Electroanal. Chem.* **1987**, *220*, 83.
[42] L. Wang, P. Lettenmeier, U. Golla-Schindler, P. Gazdzicki, N. A. Canas, T. Morawietz, R. Hiesgen, S. S. Hosseiny, A. S. Gago, K. A. Friedrich, *Phys. Chem. Chem. Phys.* **2016**, *18*, 4487.
[43] T. Reier, M. Oezaslan, P. Strasser, *ACS Catal.* **2012**, *2*, 1765.
[44] T. Reier, D. Teschner, T. Lunkenbein, A. Bergmann, S. Selve, R. Kraehnert, R. Schlogl, P. Strasser, *J. Electrochem. Soc.* **2014**, *161*, F876.
[45] L. A. Wang, R. F. Du, X. Liang, Y. C. Zou, X. Zhao, H. Chen, X. X. Zou, *Adv. Mater.* **2024**, *36*, 2312608.
[46] P. Lettenmeier, L. Wang, U. Golla-Schindler, P. Gazdzicki, N. A. Cañas, M. Handl, R. Hiesgen, S. S. Hosseiny, A. S. Gago, K. A. Friedrich, *Angew. Chem., Int. Ed.* **2016**, *55*, 742.
[47] E. A. Paoli, F. Masini, R. Frydendal, D. Deiana, C. Schlaup, M. Malizia, T. W. Hansen, S. Horch, I. E. L. Stephens, I. Chorkendorff, *Chem. Sci.* **2015**, *6*, 190.
[48] K. Talukdar, M. A. Ripan, T. Jahnke, P. Gazdzicki, T. Morawietz, K. A. Friedrich, *J. Power Sources* **2020**, *461*, 228169.
[49] L. V. Buhre, S. Bullerdiek, P. Trinke, B. Bensmann, A. L. E. R. Deutsch, P. Behrens, R. Hanke-Rauschenbach, *J. Electrochem. Soc.* **2022**, *169*, 124513.
[50] M. Komma, A. T. S. Freiberg, F. Arslan, M. Milosevic, S. Cherevko, S. Thiele, T. Böhm, *ACS Appl. Mater. Interfaces* **2024**, *18*, 23220.
[51] S. Chatterjee, X. Peng, S. Intikhab, G. S. Zeng, N. N. Kariuki, D. J. Myers, N. Danilovic, J. Snyder, *Adv. Energy Mater.* **2021**, *11*, 2101438.
[52] M. Mockl, M. F. Ernst, M. Kornherr, F. Allebrod, M. Bernt, J. Byrknes, C. Eickes, C. Gebauer, A. Moskovtseva, H. A. Gasteiger, *J. Electrochem. Soc.* **2022**, *169*, 064505.
[53] G. Mirshekari, R. Ouimet, Z. Q. Zeng, H. R. Yu, S. Bliznakov, L. Bonville, A. Niedzwiecki, C. Capuano, K. Ayers, R. Maric, *Int. J. Hydrogen Energy* **2021**, *46*, 1526.
[54] Strategic Research and Innovation Agenda 2021 –2027 https://www.clean-hydrogen.europa.eu/knowledge-management/strategy-map-and-key-performance-indicators/clean-hydrogen-jusria-key-performance-indicators-kpis_en (accessed: October 2023).
[55] J. Torrero, T. Morawietz, D. G. Sanchez, D. Galyamin, M. Retuerto, V. Martin-Diaconescu, S. Rojas, J. A. Alonso, A. S. Gago, K. A. Friedrich, *Adv. Energy Mater.* **2023**, *13*, 2204169.
[56] F. V. Linden, E. Pahon, S. Morando, D. Bouquain, *J. Power Sources* **2023**, *575*, 233168.
[57] C. Liu, M. Shviro, A. S. Gago, S. F. Zaccarine, G. Bender, P. Gazdzicki, T. Morawietz, I. Biswas, M. Rasinski, A. Everwand, R. Schierholz, J. Pfeilsticker, M. Müller, P. P. Lopes, R. A. Eichel, B. Pivovar, S. Pylypenko, K. A. Friedrich, W. Lehnert, M. Carmo, *Adv. Energy Mater.* **2021**, *11*, 2002926.
[58] K. Wegner, B. Schimmoeller, B. Thiebaut, C. Fernandez, T. N. Rao, *KONA Powder Part. J.* **2011**, *29*, 251.
[59] R. Hesse, T. Chasse, R. Szargan, *Fresen. J. Anal. Chem.* **1999**, *365*, 48.
[60] B. Ravel, M. A Newville, *J. Synchrotron Radiat.* **2005**, *12*, 537.
[61] T. Mlkow, A. Pilenga, G. Tsotridis, G. De Marco, in *Publications Office of the European Union*, European Commission, Luxembourg **2018**, JRC104045.
[62] P. Lettenmeier, S. Kolb, N. Sata, A. Fallisch, L. Zielke, S. Thiele, A. S. Gago, K. A. Friedrich, *Energy Environ. Sci.* **2017**, *10*, 2521.